ADVANCED ENERGY MATERIALS

Supporting Information

for *Adv. Energy Mater.,* DOI: 10.1002/aenm.202203873

Effect of Particle Size and Pressure on the Transport Properties of the Fast Ion Conductor *t*-Li_7SiPS_8

*Christian Schneider, Christoph P. Schmidt, Anton Neumann, Moritz Clausnitzer, Marcel Sadowski, Sascha Harm, Christoph Meier, Timo Danner, Karsten Albe, Arnulf Latz, Wolfgang A. Wall, and Bettina V. Lotsch**

Supporting Information: Effect of Particle Size and Pressure on the Transport Properties of the Fast Ion Conductor t-Li_7SiPS_8

Christian Schneider,[†] Christoph P. Schmidt,[‡] Anton Neumann,[¶,§] Moritz Clausnitzer,[¶,§] Marcel Sadowski,[‖] Sascha Harm,[⊥,†] Christoph Meier,[‡] Timo Danner,[¶,§] Karsten Albe,[‖] Arnulf Latz,[¶,§] Wolfgang A. Wall,[‡] and Bettina V. Lotsch[*,⊥,†]

†*Max Planck Institute for Solid State Research, Heisenbergstraße 1, 70569 Stuttgart, Germany*

‡*Institute for Computational Mechanics, Bolzmannstraße 15, 85748 Garching bei München, Germany*

¶*German Aerospace Center (DLR), Institute of Engineering Thermodynamic, 70569 Stuttgart*

§*Helmholtz Institute for Electrochemical Energy Storage, 89081 Ulm, Germany*

‖*Institute of Materials Science, Technical University of Darmstadt, Otto-Berndt-Straße 3, 64287 Darmstadt, Germany*

⊥*LMU Munich, Butenandstraße 5-13, 81377 Munich, Germany*

E-mail: b.lotsch@fkf.mpg.de

Crystallite Size of pristine Li_7SiPS_8

The primary particle size, i.e. the crystallite size, can be estimated from the peak broadening observed in X-ray diffraction experiments. Peak broadening is affected by the domain size and instrumental broadening (size broadening), as well as broadening by lattice strain (defects). We measured powder X-ray diffraction (see Figure S1) to compare the Bragg peak broadening of the <50 um and >50 um PSD fractions. The peaks of the <50 um sample

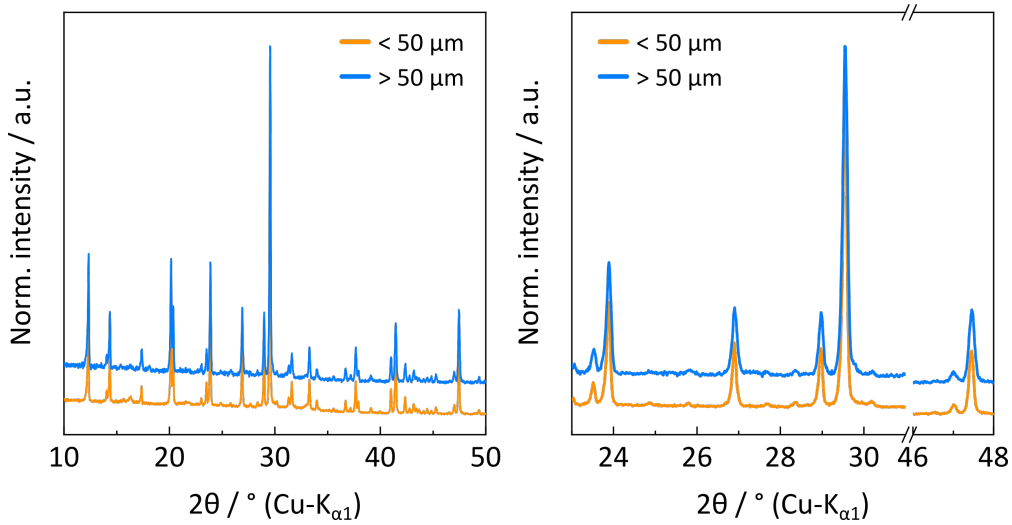

Figure S1: (a) XRD pattern of tetragonal Li_7SiPS_8 (t-Li_7SiPS_8) for the <50 um and >50 um fractions measured in Debye-Scherrer (capillary) geometry. (b) Zoomed-in XRD pattern.

are slightly broader compared to the >50 um sample, which is reflected in the FWHM and integral breadth of the five selected single peaks shown in Figure S1b. According to the Scherrer equation, a lower FMHM or integral breadth translates to a larger crystallite size. However, one needs to account for instrumental broadening, which for the used lab diffractometer (STOE StadiP) is almost on the same order as the FWHM or integral breadth of the t-Li_7SiPS_8 sample. As a reference for instrumental broadening, a Si standard (NIST 640d) was measured using the same instrument parameters. Although, a precise domain size determination by XRD is not feasible, the slightly larger FWHM of the <50 um sample indicates slightly smaller domain sizes compared to the >50 um sample.

Process of SEM image analysis using ImageJ

This section describes the workflow for analyzing gray-scale images acquired using scanning electron microscopy (SEM). SEM images can contain different information depending on the type of detector used to generate the image. While secondary electron (SE) detectors provide topographic information, back-scattered electron (BSE) detectors resolve compositional details by displaying heavier atoms brighter than lighter elements. Since the subject of this study, the solid electrolyte t-Li_7SiPS_8, is homogeneous in composition, SE images were used to analyze particle morphology and size distribution. However, for composites such as catholytes - a mixture of solid electrolyte, cathode active material, binder, and conductive additive - BSE images can help distinguish between the individual components of the mixture. Combining the analysis of SE and BSE images can improve segmentation.

The flowchart of the analysis of SEM images to determine the particle size distribution and morphology parameters is shown in Figure S2. In the following, important parts of the process and possible sources of error are described in more detail. These mainly concern the decisions that the user must make and depend on the user's experience. Since SEM images consist of individual pixels, each with a gray-scale value, the intensity of the pixel, such as brightness, can be used to determine whether a pixel belongs to the foreground or the background. For this method, the background should have a homogeneous gray value without artifacts, such as individual "high spots" (bright pixels/noise) or "shadows". Overexposure of the background can be corrected by applying a filter, such as a Gaussian blur, to the image (see Figure S3b). While this process smooths the image and reduces noise, it has the disadvantage of losing detail and blurring the boundaries between the background and particles. Therefore, the user should be careful in this processing step and try different smoothing algorithms to find the best one for the task. After preparing the image, a mask must be created to separate the background from the region of interest (ROI) by choosing an appropriate threshold (see Figure S3c). Here, only the ROI is analyzed while the background is ignored. For the analysis of particles, they must be separated. This

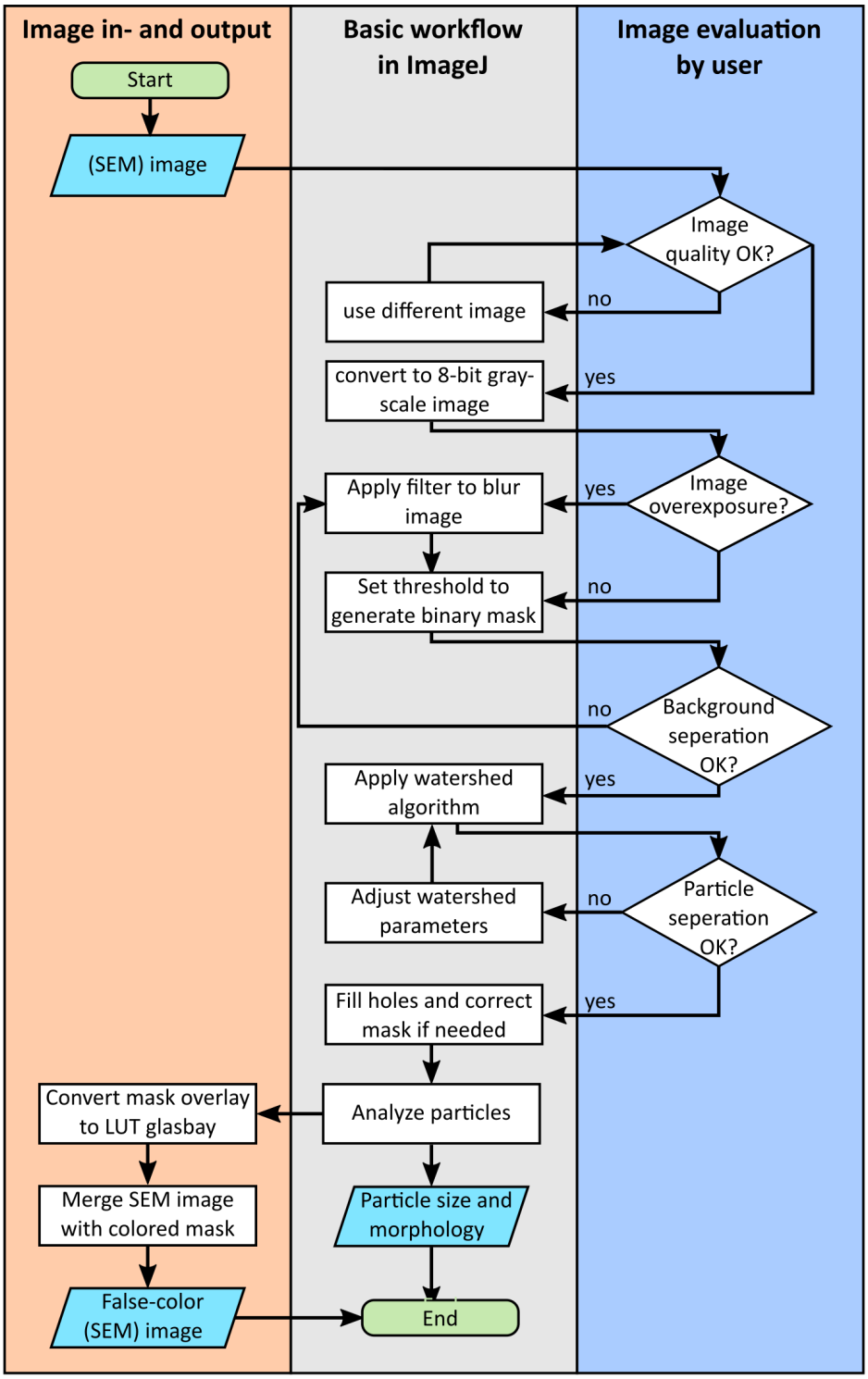

Figure S2: Flowchart of particle size and morphology analysis used in this study. Processes are displayed as rectangular boxes, decisions as diamond boxes.

can be done either by physical separation before image acquisition or by image processing. Although we finely dispersed *t*-Li_7SiPS_8 powder on the SEM sample holder, we visually observed larger agglomerates of touching particles. To digitally separate the agglomerates, the distance-transformed watershed algorithm was used as part of the MorphoLibJ[S1] plugin. This algorithm is a combination of Euclidean distance map and watershed segmentation that together results in good segmentation without oversegmentation of particles. The segmented particles are separated by either a 4-fold (pixels sharing an edge) or 8-fold (pixels sharing an edge or vertex) connected line. The type of connection can affect the roundness of objects, especially for smaller objects. It can also be a source of error for later analysis, as some algorithms interpret diagonally (8-fold connectivity) separated particles as not separated. Once the agglomerates are resolved and the remaining holes are filled, the ROI can be analyzed (see Figure S3d). Several particle counting and particle morphology algorithms are available either as a built-in function or as part of a ImageJ plugin. For this study, the plugin *morphology* by G. Landini[S2] and the built-in particle analysis tool of ImageJ were used. After analyzing the ROI, the overlaid gray-scale mask that distinguishes individual particles can be converted to a randomly colored mask (see Figure S3e), which can be used to create false-color SEM images (see Figure S3f), as shown in this paper.

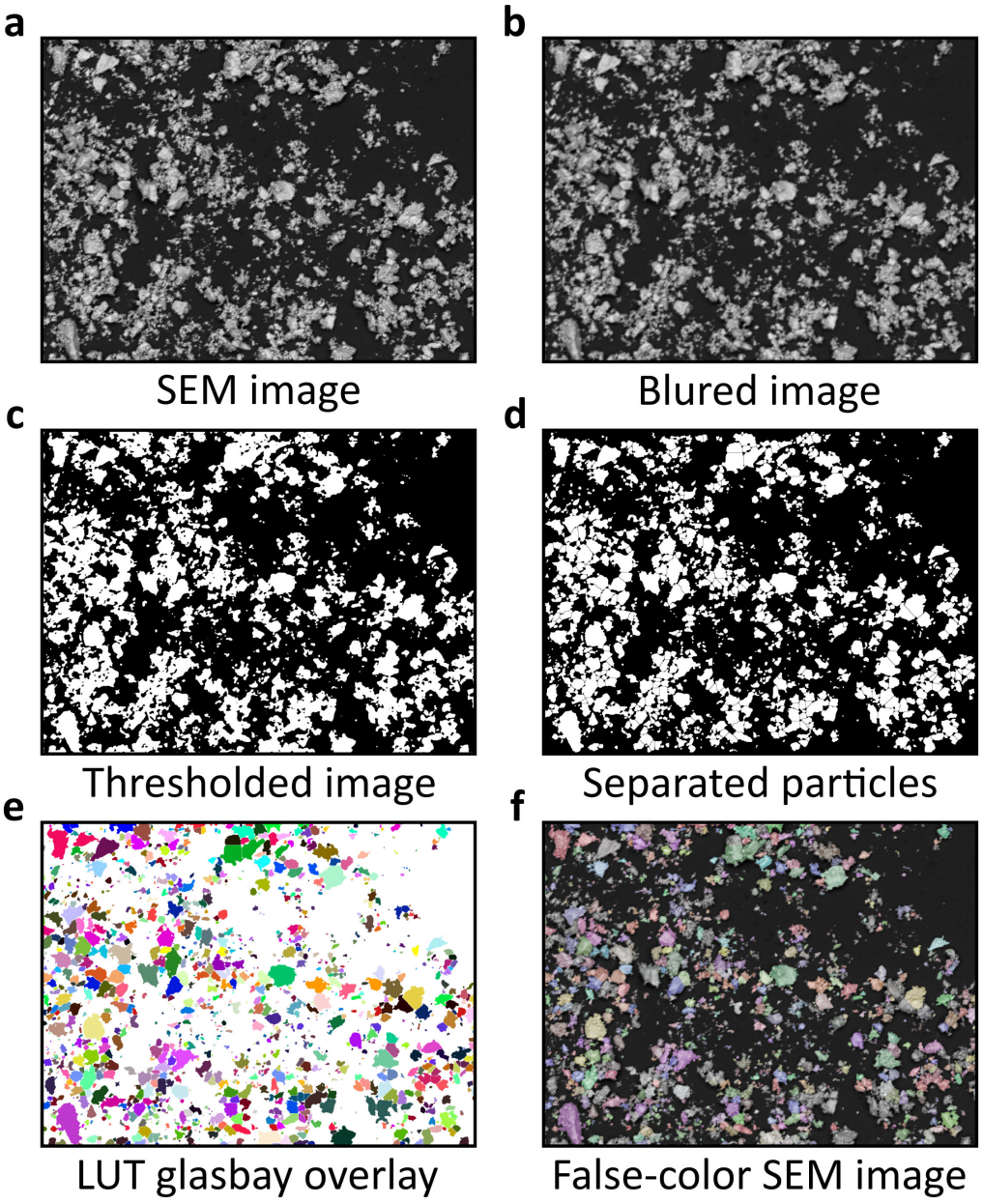

Figure S3: (a) Original SEM image, (b) after applying Gaussian blur filter, (c) binary mask after thresholding. Black and white parts denote the background and ROI. (d) Separated particles after applying distance transform watershed algorithm, (e) Colored mask showing the individual particles, and (f) False-color SEM image by merging (a) and (e).

Particle size distribution of *t*-Li_7SiPS_8

Figure S4a-c and S5a-e show SEM images with a false-color overlay used to analyze the particle sizes and shapes of the two screened size fractions. The PSD, as shown in this work, is truncated at smaller particle sizes, as a consequence of the chosen image magnification. This effect is more pronounced for the >50 µm sample, because a lower SEM image magnification was needed for this sample in order to have good count statistics while still resolving small particles compared to the respective largest ones.

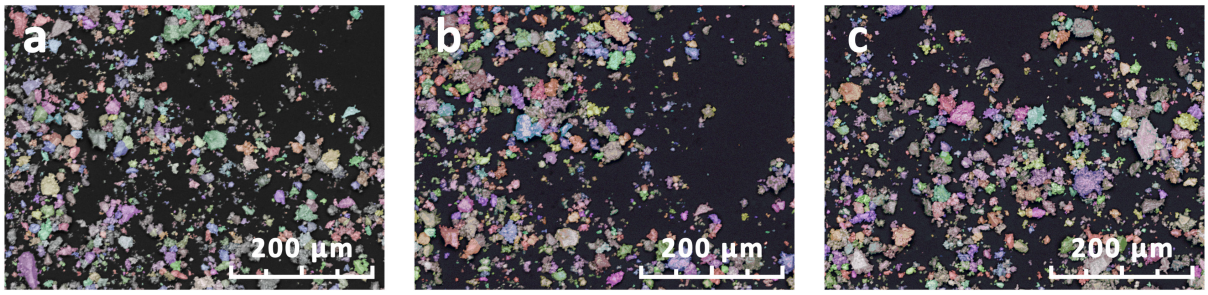

Figure S4: False-color SEM images of < 50 µm *t*-Li_7SiPS_8 particles. A total number of 3475 particles were measured.

In addition to the number-based particle size distribution measured by SEM image analysis, we used sedimentation analysis in a centrifugal field (LUMiSizer, LUM GmbH) to measure the volume-based PSD of *t*-Li_7SiPS_8. For this purpose, some powder was dispersed in a solution of *p*-xylene and 4.5 wt.% HNBR, the latter being added to adjust the viscosity. During centrifuging with increasing speed from 300 to 4000 rpm, the samples were illuminated with an 870 nm laser beam. The PSD could be calculated from the measured sedimentation velocity distribution based on known material properties such as viscosity and density. The PSD from sedimentation analysis (LumiSizer) and SEM image analysis is shown in Figure S6.

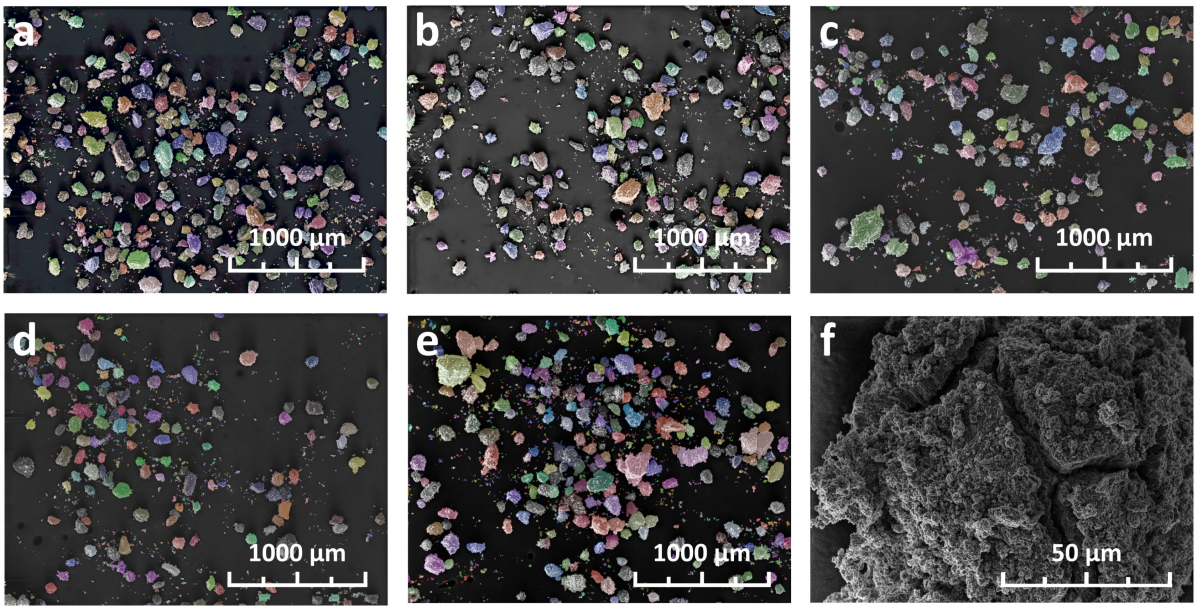

Figure S5: (a)-(e) False-color SEM images of $> 50\,\mu m$ t-Li_7SiPS_8 particles. (f) SEM image of a t-Li_7SiPS_8 particle showing the rough surface morphology observed on large particles. A total number of 5118 particles were measured.

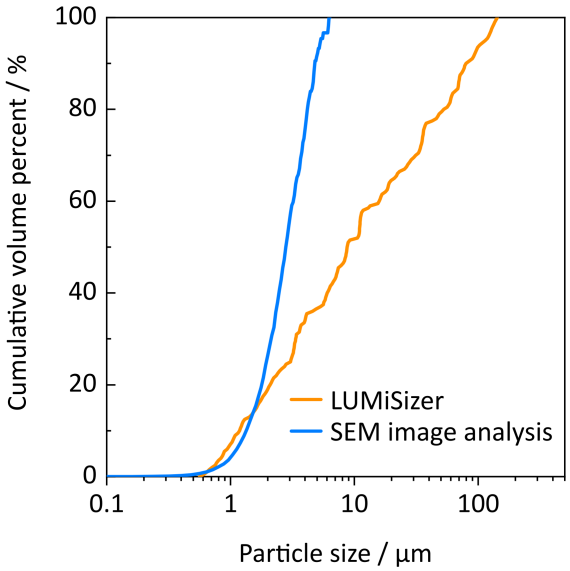

Figure S6: Cumulative volume percent as a function of particle size for the $<50\,\mu m$ sieving fraction of t-Li_7SiPS_8. The distribution curve for the SEM image analyis is calculated from the number-based distribution of Feret diameters.

The particle size parameters D_{10}, D_{50}, and D_{90}, given in table S1 and S2, describe the particle size (Feret diameter) at which 10%, 50%, and 90% of the volume- and number-based size distribution are smaller than the given value.

Table S1: Volume based size distribution parameters for *t*-Li_7SiPS_8 particle size fractions obtained by sieving. The volume based distribution was calculated from the Feret diameter.

Parameter	<50 µm	>50 µm
D_{10} / µm	17	89
D_{50} / µm	35	138
D_{90} / µm	60	240

Table S2: Number based size distribution parameters for *t*-Li_7SiPS_8 particle size fractions obtained by sieving.

Parameter	<50 µm	>50 µm
D_{10} / µm	3	9
D_{50} / µm	11	17
D_{90} / µm	27	98

Morphology of *t*-Li_7SiPS_8 particles

Parameters describing the (2D) shape of a particle must meet certain criteria.[S3] Based on these criteria, many shape descriptors have been proposed and used by researchers in different research areas. In this study, we have used some of the most popular shape descriptors, namely convexity, sphericity, circularity, and solidity. The dimensional and derived dimensionless parameters extracted from SEM image analysis using ImageJ are shown in Table S3 and Table S4, respectively.

Figure S7a shows the particle shape parameters convexity, solidity, and sphericity in a 2D scatter plot for the <50 µm particle size fraction. Most particles have quite high values of convexity and solidity, but sphericity is quite low. While sphericity correlates negatively with bumps (small inscribed circle) and positively with spikes (large circumscribed circle), solidity and convexity are more robust to star-like patterns. The 2D representations of four different particles shown in Figure S7 help to understand the concepts of convexity, solidity, and sphericity. Convexity is sensitive to the outline because it is the ratio between the perimeter of the shape and the perimeter of the smallest enclosing polygon (convex hull). It is 1 for shapes such as rectangles, spheres, or triangles, while it is close to 0 for stars. Solidity, on the other hand, is sensitive to area, as it is the ratio between the particle area and the area of the convex hull. A comparison of particles 1 and 2 from Figure S7a shows that the two dents in particle 1 caused by the elongated part result in lower solidity, while the convexity in 1 and 2 is almost identical. When the outline of the particle is more irregular and thus the circumference is longer, as in particle 3, the convexity is lower compared to particles with regular outline like 1. In this case, the solidity is not strongly affected by the irregularity in the particle outline. Particle 2 has a higher sphericity than particles 1, 3 and 4. Since sphericity describes the ratio between the radii of the inscribed and circumscribed circles, dents, grooves, or peaks directly affect these circles and thus reduces sphericity. Therefore, sphericity is a good measure of how close a 2D object is to a circle. From Figure S7a, it can be seen that *t*-Li_7SiPS_8 particles with higher convexity and solidity also have higher

sphericity values, with the latter correlating more strongly with solidity than with convexity.

The corresponding figure for the >50 µm particle size fraction is shown in Figure S8. It is evident, that the larger PSD sample also shows a broader distribution of convexity and solidity values, with values as low as 0.6 for convexity and 0.5 for solidity. However, the majority of particles have convexity and solidity values close to unity. The sphericity only shows a clear correlation with solidity but not with convexity. This trend was not observed as pronounced for the smaller PSD sample. Additionally, more particles have low sphericity as in the smaller PSD sample.

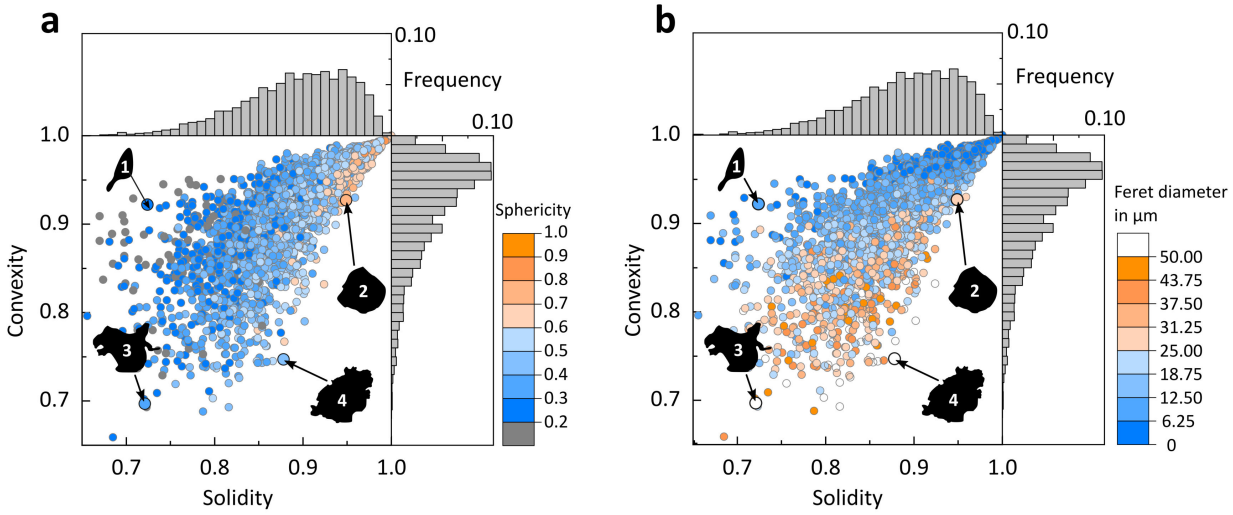

Figure S7: 2D scatterplot of particle shape, convexity and solidity, with respective marginal histograms to show the data marker density. The associated sphericity (a) and feret diameter (b) is represented by a color code as the marker infill color. 2D-representations of four particles are depicted as filled outlines. The data was measured on the <50 µm sieving fraction.

Since particle shape analysis is based on 2D representations consisting of pixels, the size of the particles, expressed here as the Feret diameter, can affect the calculation of dimensional parameters such as area and perimeter. Generally, smaller particles are more prone to artifacts because they appear "blockier" than they are. Higher magnification can mitigate this problem, but at the cost of increasing surface roughness artifacts and generally lower count statistics (see section above). Here, Feret diameter correlates negatively with convexity, a parameter sensitive to circumference (see Figure S7b). Smaller particles have

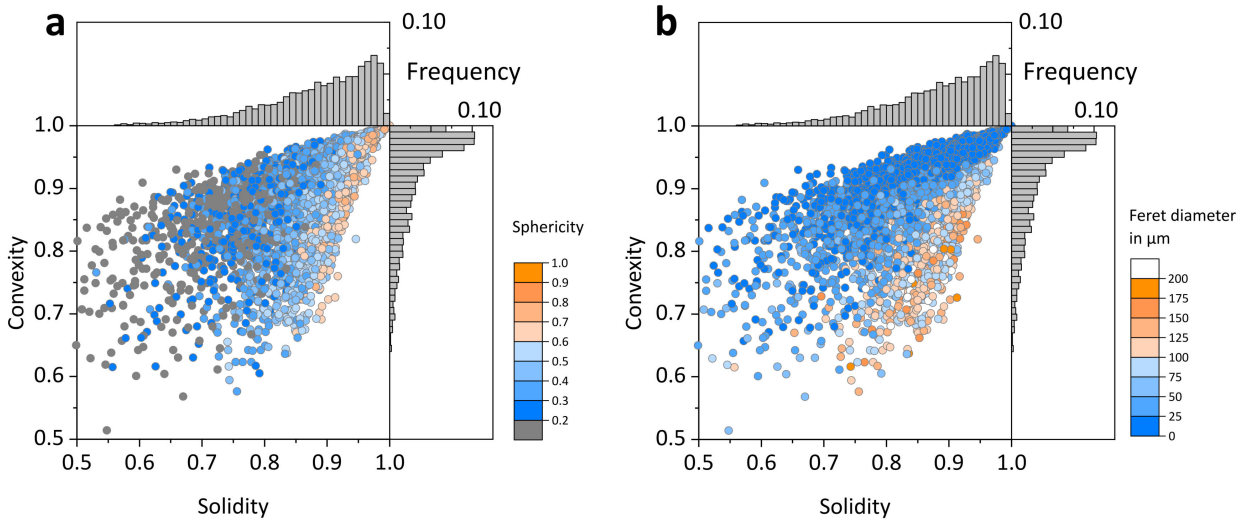

Figure S8: 2D scatterplot of particle shape, convexity and solidity, with respective marginal histograms to show the data marker density. The associated sphericity (a) and feret diameter (b) is represented by a color code as the marker infill color. 2D-representations of four particles are depicted as filled outlines. The data was measured on the >50 µm sieving fraction.

lower resolution of their respective roughness and therefore tend to have higher convexity. However, this artifact is less pronounced for solidity. Nevertheless, when analyzing particle size and shape, the magnification and resolution of the image are of great importance to the quality of the analysis. Therefore, the user should be aware of this effect and check the robustness of the morphology parameters to resolution and magnification.

Table S3: Dimensional parameters from SEM image analysis using the Morphology[S2] plugin *particles8* for ImageJ.

Parameter	Symbol	Unit	Short description
Area	A	px^2	Object's area defined by outline
Perimeter	p	px	Calculated from the boundary pixel's centers
Feret	D_{Feret}	px	Maximal distance of two parallel tangents (caliper diameter)
Breadth	$D_{Breadth}$	px	Largest diameter perpendicular to Feret
Circumscribed circle	R_{max}	px	radius of the circumscribing circle
Inscribed circle	R_{min}	px	radius of the inscribing circle
Convex hull	p_{hull}	px	Perimeter calculated from the convex hull pixel's centers
Convex area	A_{hull}	px^2	Area defined by convex hull outline

Table S4: Dimensionless parameters[S4] from SEM image analysis using the Morphology[S2] plugin *particles8* for ImageJ.

Parameter	Formula	Comment
Aspect Ratio (AR)	$\frac{D_{Feret}}{D_{Breadth}}$	A simple measure of elongation. Not variing with surface irregularities.
Circularity	$\frac{4\pi A}{p^2}$	Synonymous to *form factor*. Varies with surface irregularities.
Solidity	$\frac{A}{A_{hull}}$	Measure of how dense an object is. Objects with holes or a highly irregular boundary appear to have a low solidity.
Convexity	$\frac{p_{hull}}{p}$	Relative amount that an object differs from a concave object. Measure of how irregular an object is.
Sphericity	$\frac{R_{min}}{R_{max}}$	Measure of the degree to which an object approaches a circle. Equal to unity for a circle and close to zero for extreme star-like shapes.
Compactness	$\frac{\sqrt{\frac{4}{\pi}A}}{D_{Feret}}$	Ratio of an object's area to the area of a circle of the same perimeter. Elliptical objects or those with irregular boundaries have a low compactness.

Pellet densification of t-Li_7SiPS_8

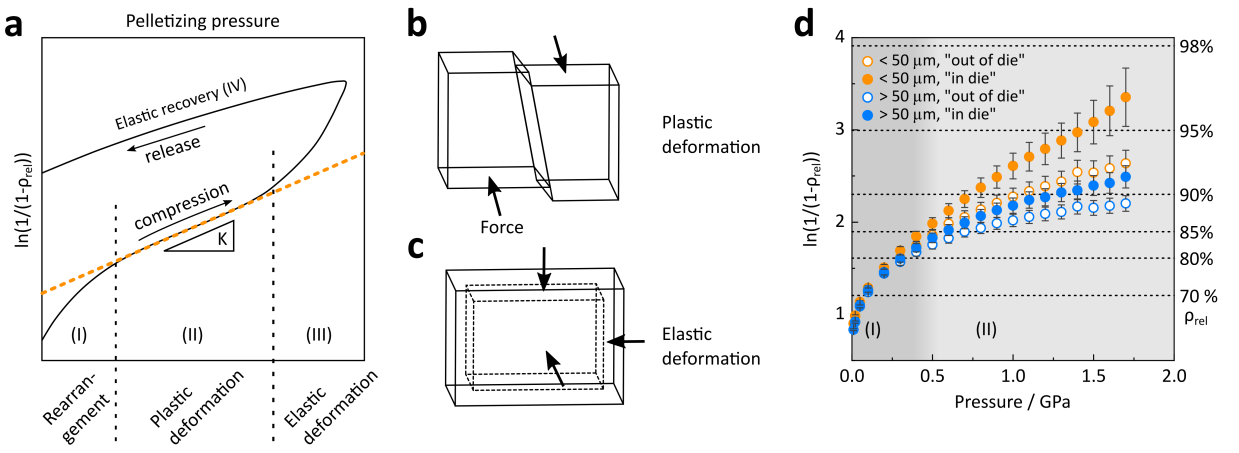

Figure S9: (a) Schematic Heckel plot with the 4 distinctive regimes dominated by particle rearrangement (I), particle plastic deformation (II), compact elastic deformation (III), and compact elastic recovery (IV). The orange, dotted line represents the linear regime of the Heckel plot. (b) Scheme of irreversible plastic deformation by shifting along a (lattice) plane. (c) Scheme of reversible elastic deformation by compressing the unit cell. (d) Heckel plots of $< 50\,\mu m$ (orange) and $> 50\,\mu m$ (blue) t-Li_7SiPS_8 samples. Hollow and filled data markers represent "out of die" and "in die" data, respectively. "Out of die" data was extracted from stack (constant) pressure experiments at 10 MPa, "in die" data was extracted at pelletizing (variable) pressure.

If the compaction of a granular powder exhibits rearrangement and/or fragmentation of the particles, a deviation from the linear Heckel plot can be observed, as indicated in region (I) in Figure S9a. The models of Cooper and Eaton,[S5] and Wünsch[S6] *et al.* attempt to provide a two-term model, including the initial (low pressure) regime of particle rearrangement/fragmentation, as well as the solid compressibility of the compact.

Comment on pellet recovery

Upon pressure release, the cracks, observed in S10, may be introduced, which could increase the tortuosity for ion conduction. In the process of pellet recovery, we have experienced that the mechanical stability of the sample is sensitive to the previously applied pressure. Since the die limits the expansion of the pellet in the axial direction, it is likely that some stress builds up on the walls of the die as the pressure is released. To press the pellet out of the

mold, the friction between the die wall and the pellet must be overcome. The stress on the walls can increase the friction, possibly leading to mechanical failure of the pellet when it is released from the die. The abrupt movement of the press bars resulted in the breaking of the pellet edges at best, but most often the pellet broke into many pieces. Taking the pellet out more slowly helped solve this problem in some cases. Notably, we observed that for some solid ion conductors (other than thiophosphates) a lower compaction pressure yielded a more stable pellet, while higher pressures led to mechanical failure of the pellet during recovery from the die. This might be caused by a large elastic recovery of some materials building up internal stress.

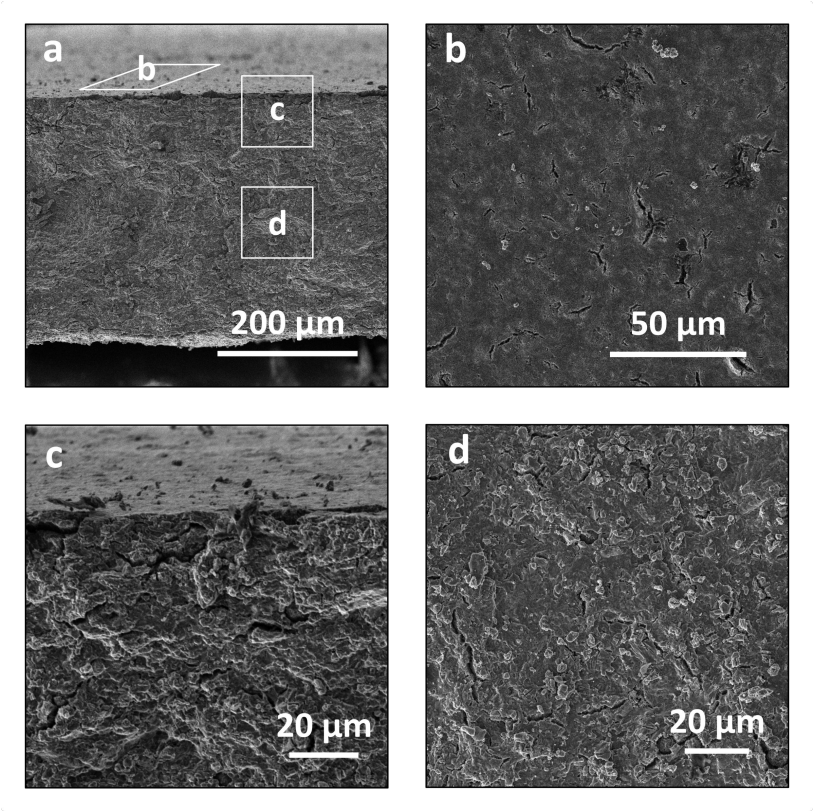

Figure S10: SEM images of t-Li_7SiPS_8. (a) Broken cross-section of the pellet, (b) surface of the pellet, (c) broken cross-section close to the pellet's surface and (d) in the middle of the pellet.

Nyquist plots

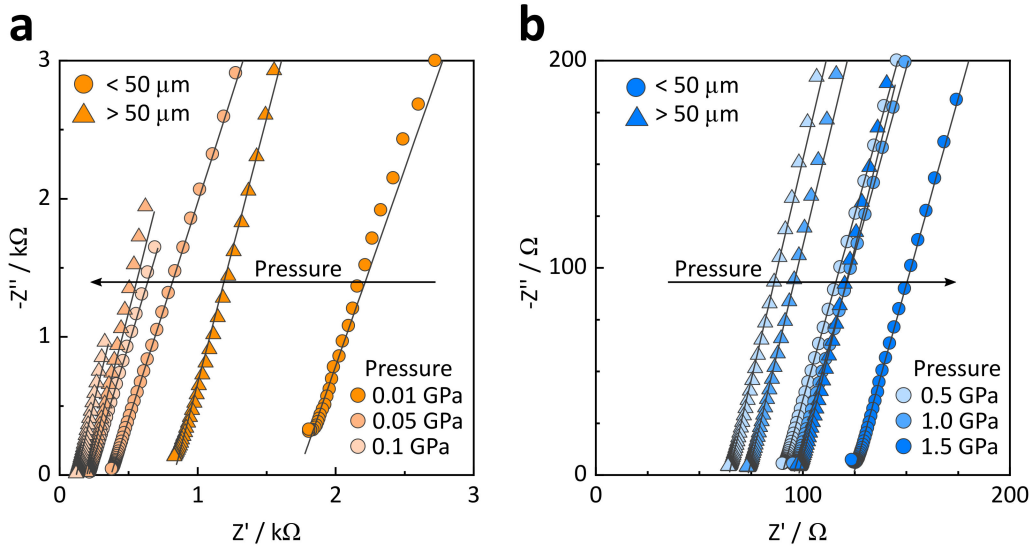

Figure S11: Nyquist plots of t-Li_7SiPS_8 at low (a) and high (b) pelleting pressures. The circle and triangle data markers represent the < 50 and $> 50\,\mu m$ particle size fractions, while the fill color represents the pelleting pressure.

Derivation of Activation Volume

Similar to the effect of temperature on diffusion, which is a temperature-activated process following an Arrhenius law, thermodynamic laws allow the definition of an activation volume ΔV. Here, we briefly review the thermodynamics of ion diffusion and the definition of the activation volume. The ionic conductivity of solids can be described as a thermally activated process following an Arrhenius behavior:

$$\sigma T = \sigma_0 e^{\frac{-\Delta G}{k_B T}} \tag{1}$$

During diffusion, mobile ions must overcome the Gibbs free energy ΔG to jump from one lattice site to an adjacent one. Solving equation (1) for ΔG and assuming a closed system with the number of particles N of chemical potential i (N_i = const.) at a constant temperature (T = const.), we obtain:

$$\Delta G = k_B T \left(\ln(\sigma_0)_{T,N_i} - \ln(\sigma)_{T,N_i}\right). \tag{2}$$

Equation (1) includes the pre-exponential factor σ_0, that is defined as:

$$\sigma_0 = \frac{z n q^2 r^2 \nu_0}{k_B}, \tag{3}$$

with z, n, q, r, and ν_0 being a geometrical factor, the number of charge carriers per unit volume, the charge (*e.g.* for Li^+ $q = 1$), the "jump" distance between two neighbouring sites, and the attempt frequency, respectively.

Assuming z, n, and q to not change with pressure, equation (2) can be written as:

$$\Delta G = k_B T \left(\ln(r)_{T,N_i} + \ln(\nu_0)_{T,N_i} - \ln(\sigma)_{T,N_i}\right) \tag{4}$$

It follows, that the Gibbs free energy ΔG depends on the jump distance, the attempt frequency and the conductivity. The partial derivative of ΔG with pressure is defined as the activation volume ΔV:

$$\left(\frac{\partial \Delta G}{\partial p}\right)_{T,N_i} = \Delta V \tag{5}$$

Combining equation (2) and (5) gives:

$$\Delta V = k_\mathrm{B} T \left(\left(\frac{\partial \ln(\sigma_0)}{\partial p}\right)_{T,N_i} - \left(\frac{\partial \ln(\sigma)}{\partial p}\right)_{T,N_i} \right) \tag{6}$$

While the variation of conductivity with pressure is readily available through experimentation, it is much more difficult to obtain information on the pressure variance of the jump distance and attempt frequency that contribute to the pre-exponential factor. Some approximations and simplifications can be found in the literature. In a cubic crystal system, for example, this correction term can be estimated by the compressibility β and the Grüneisen constant γ:[S7–S10]

$$\Delta V = k_\mathrm{B} T \left(\beta \left(\gamma - \frac{2}{3}\right) - \left(\frac{\partial \ln(\sigma)}{\partial p}\right)_{T,N_i} \right) \tag{7}$$

^{31}P-NMR of pristine and pressed t-Li_7SiPS_8

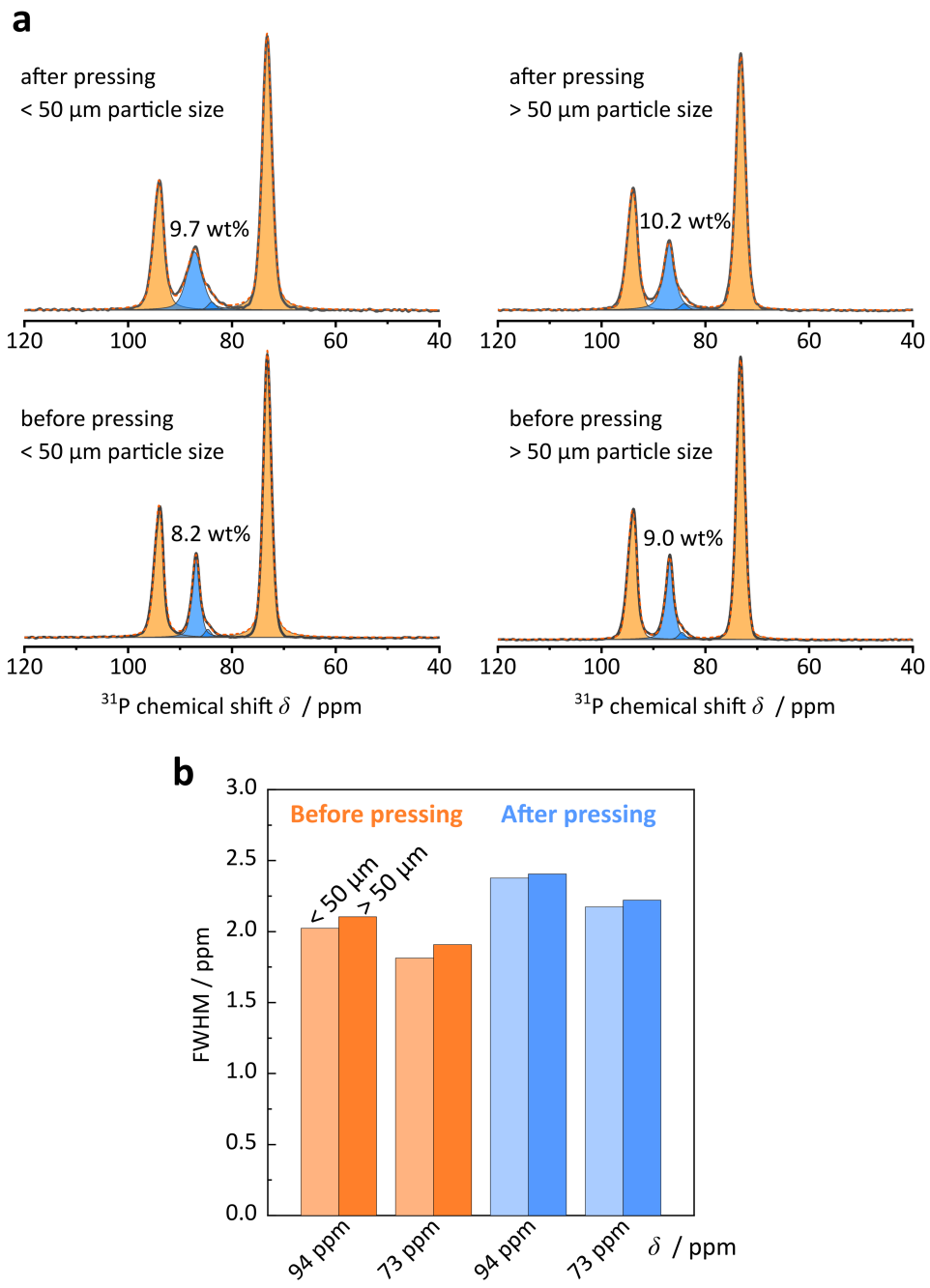

Figure S12: (a) ^{31}P MAS NMR spectra of pristine and pressed t-Li_7SiPS_8 of different particle size fractions. Peaks attributed to crystalline t-Li_7SiPS_8 and to the amorphous side phase are depicted in orange and blue, respectively. The fit is displayed as an orange, dashed line. The measured data is depicted as a dark gray line. (b) Full width half maximum (FWHM) of ^{31}P MAS NMR t-Li_7SiPS_8 peaks.

Discrete element method simulation

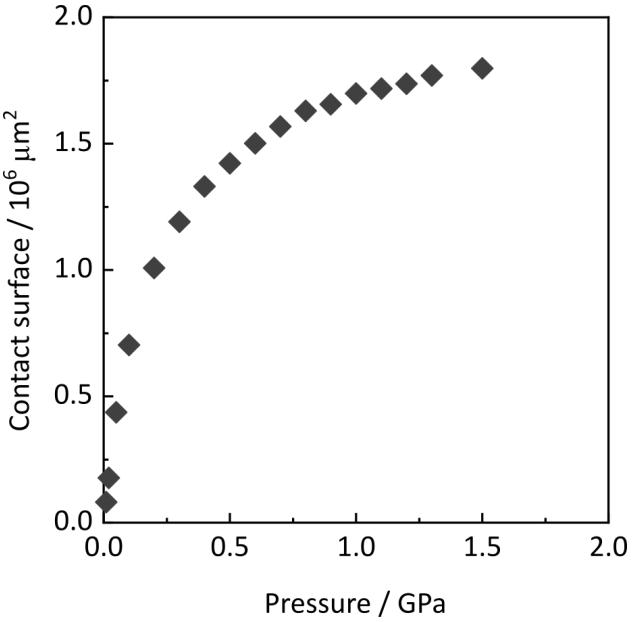

Figure S13: Contact surface as a function of the pelletizing pressure.

In the DEM simulation the compaction of perfect spheres attributed with friction effects, form the pellet. The solid electrolyte powder, however, consists of particles that are far from spherical. They rather have various morphological features, such as holes, jags, dips, and bulges, which contribute to surface roughness (see for example Figure S7). This can increase friction by causing the particles to coalesce into larger agglomerates that require higher stress to break up. Additionally, surface roughness can introduce current constriction effects[S11–S13] at the inter-particle contacts, especially, when the particles are not allowed to connect at low pressure. Fleig has shown that a larger number of inter-particle contact spots give rise to a smaller current constriction effect and thus a smaller grain-boundary resistance.[S11] At a higher compression stage, the number of contact surface increases, as shown in Figure S13.

Methods

Synthesis and Sample preparation

Tetragonal Li_7SiPS_8 (t-Li_7SiPS_8) was prepared from a stoichiometric mixture of Li_2S (Sigma Aldirch, 99.98%), red phosphorus (Merck, 99%) and sulfur (sublimed). An excess of 5 wt% sulfur was added to the mixture to ensure an oxidizing reaction atmosphere during the synthesis. The starting mixture (10 g) was ball-milled using a Retsch PM 200 ball mill with 50 mL ZrO_2 jar and 10 ZrO_2 balls of 10 mm diameter. The ball mill was programmed to mill for 24 h at 500 rpm, with 5 min milling and 1 min cooling down pause. The homogenized mixture was placed in glassy carbon crucibles and subsequently sealed in quartz glass ampules under vacuum. The ampules were transferred to a tube furnace and heated to 525 °C at a rate of 50 K min^{-1}, annealed for 100 h, and naturally cooled down by switching of the furnace. The crystalline powder is pale-yellow colored and sensitive to moisture. The samples and cells were thus prepared and stored in an Argon filled glovebox (($p(O_2)/p < 5$ ppm, $p(H_2O)/p < 5$ ppm). Pristine t-Li_7SiPS_8 powder was sieved using a 50 µm mesh size sieve to yield particle fraction, one with particle sized smaller than 50 µm and one with particles larger than 50 µm. The sieve was placed on a vortex mixer to facilitate the powder sieving by vibration. This was done until visually no more powder accumulated at the bottom of the sieving pan. The powder that passed the 50 µm mesh size sieve is denoted the < 50 µm fraction, while powder that remained in the sieve after the sieving process is denoted the > 50 µm fraction. Although the > 50 µm fraction has a greater number of particles below 50 µm, the volume of the sample is dominated by particles larger than 50 µm.

Scanning Electron Microscopy

Scanning electron microscopy images were taken with a VEGA TS 5130 MM microscope (equipped with an *Oxford* X-MaxN 20 (SDD) detector) or a TESCAN VEGA4 LMU microscope. The samples were prepared by scattering little amounts of t-Li_7SiPS_8 powder

on a sticky carbon tape. Images were taken of areas at which individual particles were evenly spread out to ensure better image analysis. The particles were analysed using the software *ImageJ*[S14] and the plugins *MorphoLibJ*[S1] and *Morphology*[S2] by G. Landini. A more detailed description of the particle segmentation and size analysis can be found in the electronic supporting information (see above).

Gas Pycnometer

The true density of *t*-Li_7SiPS_8 was measured with a *micromeritics* AccuPyc II 1340 gas pycnometer using Helium gas. A weighed amount of *t*-Li_7SiPS_8 powder was placed in an aluminium crucible and subsequently transferred to the gas pycnometer. The analysis chamber was purged 10 times with Helium prior to the measurement. The accessible analysis chamber volume was measured 10 times (10 s of equilibration time) per sample and the mean density of the sample was calculated from the volume displacement and the sample weight. An average of four samples was used as the reference density for the calculation of relative pellet density. The density of *t*-Li_7SiPS_8 powder was measured to be 2.008(6) g cm^{-3}, while the reported crystallographic density is 1.923(9) g cm^{-3}.[S15] The experimentally determined density is by 4.4 % larger that the reported one. This difference is small and might originate from measurement and weighting uncertainties.

Nuclear Magnetic Resonance

^{31}P solid-state NMR measurements were performed on a Bruker Avance-III wide bore spectrometer in a magnetic field of 9.4 T. The powder sample was loaded into a pyrex MAS insert (Wilmad Glass, product # DWGSK2576-1), flame sealed and subsequently transferred into a 4 mm ZrO_2 rotor. The ^{31}P spectra (Larmor frequency 161.9 MHz) were recorded using a Bruker BL4 MAS probe at a spinning speed of 10 kHz. A simple Bloch Decay excitation scheme with a total of 512–4096 accumulations in each experiment was used. The relaxation delay was chosen long enough to allow for complete relaxation of the magnetization and to

ensure a quantitative measurement. The spectra are referenced against the external signal of 85 %H_3PO_4 [S16] and were fitted using the Dmfit [S17] software.

Variable Pressure Measurements

For the variable pressure measurements, *CompreCell* cells (RHD INSTRUMENTS) were used. The cells are comprised of an electrically insulating Al_2O_3 cylinder in a stainless steel liner. Hard metal pistons of 6 mm diameter apply the uniaxial force onto the sample, while also serving as the electrodes. The cell was loaded with 50 mg of sieved *t*-Li_7SiPS_8 powder. A double O-ring design ensures an air-tight seal for inert atmosphere conditions during the experiments. The cell was inserted into a *CompreDrive* press (RHD INSTRUMENTS) and connected to a potentiostat in a two-electrode configuration. The *CompreDrive* system allows for constantly monitoring the applied force and actively controlling the pressure. The information about the motor position can be used to calculate the displacement of the hard metal piston at each pressure step and thus the pellet thickness. A reference run without sample was performed prior to the compaction experiment to later subtract the influence of setup deformation during the high pressure experiment. The temperature was controlled using a *Julabo Presto A40* thermostat connected to heating/cooling mantle housing the cell.

Electrochemical Impedance Measurements

Prior to measuring the electrochemical impedance of *t*-Li_7SiPS_8, the potentiostat was calibrated using a load-short (100 Ω-shorted cell) calibration. The impedance spectra were recorded at 25 °C in a frequency range of 1 MHz to 100 Hz and with an applied voltage of $V_{RMS} = 10$ mV. The spectra interpretation was performed using the RHD INSTRUMENTS software package RelaxIS 3. Kramers-Kronig relation tests were performed prior to fitting to check for the reliability of the measured data. All data points were proportionally weighted during the fitting process to an equivalent circuit. The spectra were mostly fitted in the frequency range of 1 MHz to 1 kHz, however, depending on the pressure, adjustments had to

be made to avoid unmeaningful fits. Error bars originate from error propagation calculated from uncertainties in pellet thickness and fitting error. The spectra were fitted using an equivalent circuit composed of a resistor in series with a constant phase element, accounting for the ionic resistance and the polarization spike at lower frequencies.

DEM and FV Simulation

As already discussed in the introduction, we expect the mesostructural compaction of the powder to be the dominant effect in the low pressure regime. The discrete element method (DEM) is a common tool to model such effects as it enables to incorporate the crucial phenomena of powder compaction, i.e. the particle-particle and particle-wall interactions. Thus, we decided to employ DEM simulations to verify the hypothesis that powder compaction is indeed the dominant effect in this pressure regime.

The applied model is based on our previous work in the field of additive manufacturing.[S18,S19] It is premised on the DEM, as proposed by Cundall and Strack,[S20] where the particles are described as rigid spheres. Therefore, the kinematics of each particle are completely described by the position vector of the center of gravity $\boldsymbol{r}_\mathrm{G}$ as well as the angular velocity vector $\boldsymbol{\omega}$. To mathematically describe the position and rotation we incorporate the balance of linear and angular momentum of an individual particle i:

$$(m\ddot{\boldsymbol{r}}_\mathrm{G})^i = m^i\boldsymbol{g} + \sum_j \left(\boldsymbol{f}_\mathrm{CN}^{ij} + \boldsymbol{f}_\mathrm{CT}^{ij}\right), \tag{8}$$

$$(I_\mathrm{G}\dot{\boldsymbol{\omega}})^i = \sum_j \left(\boldsymbol{r}_\mathrm{CG}^{ij} \times \boldsymbol{f}_\mathrm{CT}^{ij}\right), \tag{9}$$

where the particle mass is defined as $m = 4/3\pi r^3\rho$, and the moment of inertia with respect to the center of gravity of the particle is denoted by $I_\mathrm{G} = 0.4mr^2$. Additionally, $\boldsymbol{g}$ represents the gravitational acceleration, $\boldsymbol{f}_\mathrm{CN}^{ij}$, and $\boldsymbol{f}_\mathrm{CT}^{ij}$ symbolize the interaction forces of particles i and j in normal, and tangential direction, respectively. Finally, the vector from the centroid of particle i to the contact point with particle j is delineated as $\boldsymbol{r}_\mathrm{CG}^{ij} = \boldsymbol{r}_\mathrm{C}^{ij} - \boldsymbol{r}_\mathrm{G}^{i}$. Additionally,

we need to define the contact laws to model the interaction between particles.

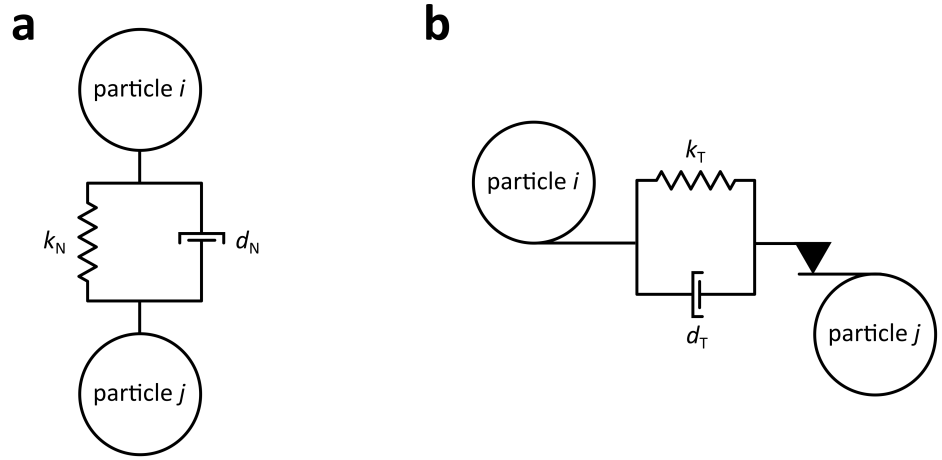

Figure S14: Sketches of normal as well as tangential contact laws applied to the particle pair i, j. (a) Schematic of the spring-dashpot model applied as normal contact law. (b) Schematic of Coulomb's law of friction applied as tangential contact law.

Figure S14 shows sketches of the applied contact laws in both normal and tangential directions. In normal direction a typical spring-dashpot model is employed:

$$\boldsymbol{f}_{\mathrm{CN}}^{ij} = \begin{cases} \min\left(0, k_{\mathrm{N}} g_{\mathrm{N}} + d_{\mathrm{N}} \dot{g}_{\mathrm{N}}\right) \boldsymbol{n}, & g_{\mathrm{N}} \leq 0 \\ \boldsymbol{0}, & g_{\mathrm{N}} > 0, \end{cases} \tag{10}$$

with the normal gap between the contacting particles $g_{\mathrm{N}} = \|\boldsymbol{r}_{\mathrm{G}}^{j} - \boldsymbol{r}_{\mathrm{G}}^{i}\| - (r^{j} + r^{i})$ and the corresponding unit normal vector $\boldsymbol{n} = \left(\boldsymbol{r}_{\mathrm{G}}^{j} - \boldsymbol{r}_{\mathrm{G}}^{i}\right) / \|\boldsymbol{r}_{\mathrm{G}}^{j} - \boldsymbol{r}_{\mathrm{G}}^{i}\|$.[S21,S22] The case distinction in (10) ensures that contact forces are only applied if a pair of particles i, j is in contact ($g_{\mathrm{N}} \leq 0$). Furthermore, k_{N} denotes the elastic normal contact stiffness and d_{N} the damping constant in normal direction. The latter calculates as:

$$d_{\mathrm{N}} = 2 \left|\ln\left(c_{\mathrm{COR}}\right)\right| \sqrt{\frac{k_{\mathrm{N}}\, m_{\mathrm{eff}}}{\ln\left(c_{\mathrm{COR}}\right)^{2} + \pi^{2}}}, \tag{11}$$

where c_{COR} represents the coefficient of restitution and $m_{\mathrm{eff}} = m^{i} m^{j} / \left(m^{i} + m^{j}\right)$ denotes an effective mass of the contacting particle pair.

Finally, the tangential contact law is based on Coulomb's law of friction:

$$\boldsymbol{f}_{\mathrm{CT}}^{ij} = \begin{cases} \min\left(\mu\|\boldsymbol{f}_{\mathrm{CN}}^{ij}\|, \|k_{\mathrm{T}}\boldsymbol{g}_{\mathrm{T}} + d_{\mathrm{T}}\dot{\boldsymbol{g}}_{\mathrm{T}}\|\right)\boldsymbol{t}_{\mathrm{T}}, & g_{\mathrm{N}} \leq 0 \\ \boldsymbol{0}, & g_{\mathrm{N}} > 0, \end{cases} \tag{12}$$

with the friction coefficient μ as well as the constants for tangential contact $d_{\mathrm{T}} = d_{\mathrm{N}}$ and $k_{\mathrm{T}} = (1-\nu)/(1-0.5\nu)k_{\mathrm{N}}$ using Poisson's ratio ν. Moreover, the time derivative of the tangential gap vector is defined as:

$$\dot{\boldsymbol{g}}_{\mathrm{T}} = \left(\boldsymbol{I} - \boldsymbol{n}\otimes\boldsymbol{n}^{T}\right)\left(\boldsymbol{v}_{\mathrm{G}}^{i} - \boldsymbol{v}_{\mathrm{G}}^{j}\right) + \omega^{i}\times\boldsymbol{r}_{\mathrm{CG}}^{ij} - \omega^{j}\times\boldsymbol{r}_{\mathrm{CG}}^{ji}, \tag{13}$$

where $\boldsymbol{I}$ denotes the identity tensor. Please note that the tangential gap vector $\boldsymbol{g}_{\mathrm{T}}$ is not uniquely defined by the geometric configuration. Instead, it is computed by numerical integration of (13). Furthermore, the unit tangent vector $\boldsymbol{t}_{\mathrm{T}}$ is calculated as:

$$\boldsymbol{t}_{\mathrm{T}} = -\frac{k_{\mathrm{T}}\boldsymbol{g}_{\mathrm{T}} + d_{\mathrm{T}}\dot{\boldsymbol{g}}_{\mathrm{T}}}{\|k_{\mathrm{T}}\boldsymbol{g}_{\mathrm{T}} + d_{\mathrm{T}}\dot{\boldsymbol{g}}_{\mathrm{T}}\|}. \tag{14}$$

The parameters listed in S5 have been used to perform the DEM simulations.

Table S5: Parameters used for the DEM simulations.

Symbol	Value	Unit	Short description	Source / Comment
ρ	1980.0	$\frac{\mathrm{kg}}{\mathrm{m}^3}$	Density	Averaged value from four batches (see section 'Gas Pycnometer')
ν	0.3	–	Poisson's ratio	Typical value for argyrodite and LGPS-type thiophosphates (see Table S7)
k_N	0.01	$\frac{\mathrm{N}}{\mathrm{m}}$	Normal contact stiffness	In DEM simulations it is common not to use the original Young's modulus as a basis for the particle stiffness, but to reduce the value for reasons of numerical efficiency.[S18,S23–S25] We follow the same approach here, justified by the fact that we are not interested in the resulting global reaction force, but only in the resulting particle morphology. However, this is not affected by the exact value of the stiffness.
c_cor	0.1	–	Coefficient of restitution	Since we are only interested in the static equilibrium after compression, i.e., the final pellet morphology, the value has negligible effect on the solution. It was chosen non-zero to dissipate energy in addition to the friction effects to save computational resources.
μ	1.0	–	Friction coefficient	Typical friction coefficients are in the range of 0.05-2.0 depending on the material pairing.[S26] Since we do not have further information on that we used a value from the middle of the range.
$\boldsymbol{g}$	$(0,0,0)^T$	$\frac{\mathrm{m}}{\mathrm{s}^2}$	Gravitational acceleration	Neglected since influence is several orders of magnitude lower compared to that of the compression as proven in a brief calculation. 50 mg of powder in a cylindrical shape of 6 mm diameter results in the following pressure due to gravity: $\frac{m_\mathrm{Smaple}}{A_\mathrm{Smaple}} \cdot g = \frac{50\,\mathrm{mg}\cdot 4}{(6\,\mathrm{mm})^2\pi} \cdot 9.81 \frac{\mathrm{N}}{\mathrm{kg}} = 17.3\,\mathrm{Pa}$ In comparison to at least 0.01 GPa external pressure this is negligible.
a	1.944	–	Gamma distribution parameter a	Fit to experimental data (see Fig. 6a)
b	1.944	–	Gamma distribution parameter b	Fit to experimental data (see Fig. 6a)

Based on the results from the DEM-simulations, finite volume (FV) simulations were conducted on the particle microstructures to determine the effective ionic conductivities of the compressed electrolyte pellets. First, from the known particle positions and diameters in the compressed samples, voxel-based microstructures with a voxel size of 1 µm were generated. Then, the simulation environment BEST (Battery and Electrochemistry Simulation Tool)[S27,S28] was used to calculate the effective conductivity of the pellets by simulating the steady state current j for an applied voltage difference of $U = 1\,\mathrm{V}$. Essentially solving the Poisson equation for the electrolyte phase allows to evaluate the mean current density at the boundary of the computational domain. For an electrolyte pellet with the thickness l_i, the effective conductivity can be calculated according to equation (15):

$$\sigma_{\mathrm{eff,i}} = l_i \cdot \frac{j}{U} \tag{15}$$

To allow for a comparison of calculated and measured conductivities, the calculated conductivities were normalized to the maximum value $\sigma_{\mathrm{eff,max}}$.

In order to consider the atomistic effect of the activation volume, the bulk conductivity of the electrolyte was reduced with increasing pressure. For each pressure level p_i corresponding to a certain pellet thickness, the bulk conductivity σ_i can be calculated from a reference state according to equation (16), which was derived from the simplified expression of the activation volume (equation (4) in main publication). However, due to the normalization of the simulated conductivities, the values in Figure 6b in the main text do not depend on the assumed bulk conductivity but only on the geometric properties of the pellet microstructure.

$$\sigma_i = e^{\ln \sigma_{\mathrm{ref}} - \frac{\Delta V}{k_{\mathrm{B}} T}(p_i - p_{\mathrm{ref}})} \tag{16}$$

In the FV-simulations the electrolyte material was treated as a homogeneous phase without

any additional grain boundary resistances between individual particles.

DFT and AIMD Simulations

Density Functional Theory (DFT) and *ab-initio* molecular dynamics (AIMD) simulations have been performed using the The Vienna Ab initio Simulation Package (VASP).[S29–S32] The PBE exchange-correlation functional[S33] and projector augmented wave pseudopotentials[S34,S35] as shipped with VASP have been used. Total energy calculations and structural relaxations were performed with a k-spacing of $0.25\,\text{Å}^{-1}$ and an energy cutoff of the plane-wave basis set of 600 eV until the electronic structure and forces were converged within $10 \cdot 10^{-6}$ eV and $0.01\,\text{eV}\,\text{Å}^{-1}$, respectively. For the determination of elastic constants, the cutoff energy was increased to 900 eV. AIMD simulations were performed in the NVT ensemble using the default cutoff energy of 499 eV, only including the gamma-point, with time steps of 1 fs, and using the Nosé-Hoover thermostat. Based on the slope of the mean-squared-displacements (MSD) of Li ions, tracer diffusion coefficients D have been determined.

2×2×1 supercells (12 formula units) of t-Li_7SiPS_8 have been used in all simulations and the supercell program[S36] was utilized to first occupy the shared Si/P sites, from which seven explicit arrangements were considered (see Figure S15). Next, Li was distributed among its partially occupied sites in several steps and the structure with the lowest electrostatic energy was used as basis for the next step. After merging pairs of Li1-Li1 sites (fully occupied), the supercell program was used to occupy 87.5% and 62.5% of the Li2 and Li4 sites simultaneously. Finally, 87.5% of the Li3 sites were occupied.

Structural Models for DFT/AIMD simulations

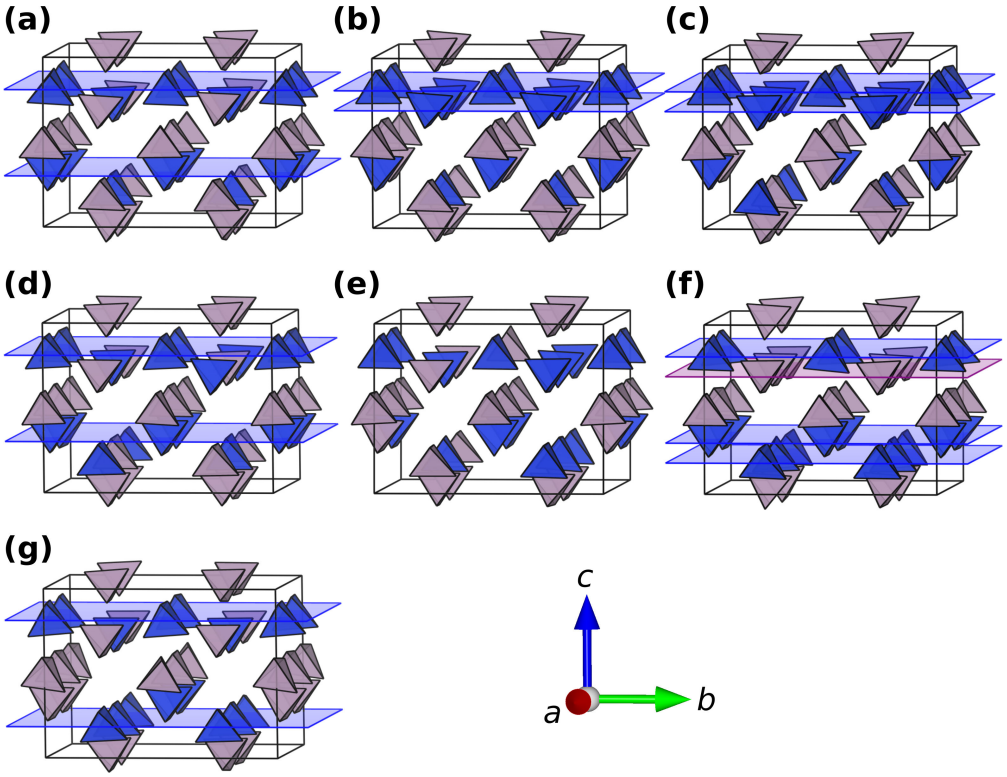

Figure S15: Structural models of t-Li_7SiPS_8 that have been used for DFT and AIMD simulations. For clarity, only PS_4^{3-} (purple) and SiS_4^{4-} (blue) tetrahedra are shown. Planes have been added as a guide to the eyes and indicate layers that are occupied by the same type of tetrahedra.

Molecular dynamics simulation

For LGPS, the structural archetype to t-Li_7SiPS_8, AIMD[S37] and single crystal impedance spectroscopy[S38] hint for a weak anisotopic conductivity, while PFG-NMR points more to isotropic ion conduction. Based on the reported crystal structure[S15] (see Figure 4a), we have calculated an activation barrier based on the bond valence sum approach[S39–S41] of 0.22 eV for 1D ion migration along the c direction and 0.28 eV for 3D migration. Additionally, we performed AIMD simulations of several explicit arrangements of the PS_4^{3-}/SiS_4^{4-} anions to calculate tracer diffusion coefficients of lithium via an analysis of the MSD. The diffusivity of lithium along c is on average four times higher than in the a/b direction (see Figure S17). This finding agrees well with the four times higher conductivity in [001] direction compared to [110] measured with single crystal impedance spectroscopy.[S38] This anisotropy is also reflected in a higher activation barrier of about 155 meV in the a/b, compared to 127(13) meV in the c direction (see Figure S18). The activation barrier derived from the total MSD amounts to 136(13) meV, fitting to the trend of the bond valence sum results. The AIMD activation barriers are lower than measured barriers in other sulfide solid electrolytes and we attribute this discrepancy to the shortcomings of extracting activation barriers from AIMD simulations at high temperatures.[S42] Moreover, the simulations represent the single crystal properties and do not consider grain boundiers or (amorphous) side phases.

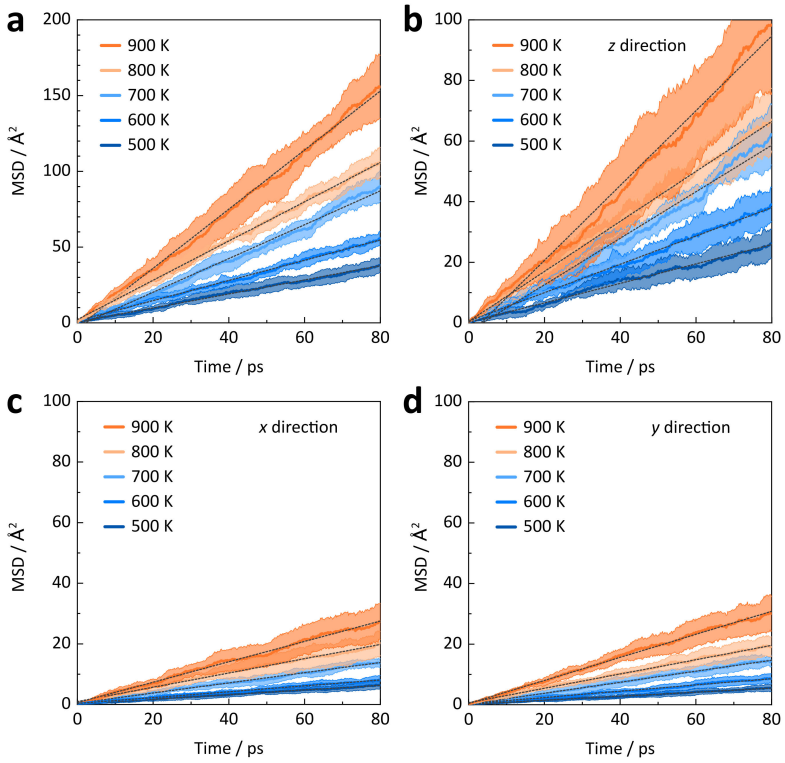

Figure S16: (a) Averaged total Mean squared displacement (MSD) of lithium from AIMD simulations at different temperatures, in comparison to the individual spatial contributions of the (b) z, (c) x, and (d) y directions. The x, y, and z directions align with the crystallographic a, b, and c direction.

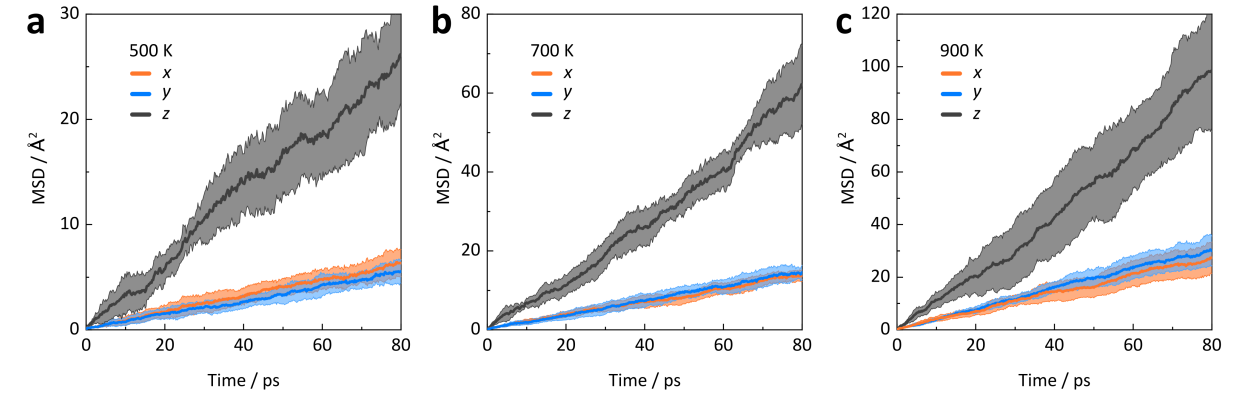

Figure S17: Mean squared displacement (MSD) of lithium at MD simulation temperatures of (a) 500 K, (b) 700 K, and (c) 900 K. The x, y, and z directions align with the crystallographic a, b, and c direction.

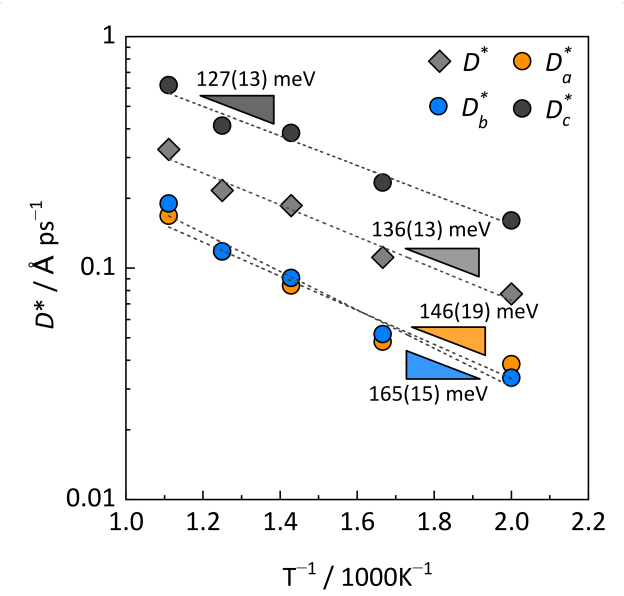

Figure S18: Arrhenius plot of the total lithium tracer diffusion coefficient (diamond, light gray), and its individual contributions along the crystallographic a, b and c directions.

Elastic properties

We calculated the volume-energy curves for the different structural models and fitted them to the Birch-Murnaghan equation of state.[S43,S44] An average bulk modulus of 22.8 GPa is obtained. Additionally, the full elastic tensor of t-Li_7SiPS_8 was calculated (see Table S6) and a bulk modulus of 23.5 GPa within the Reuss-Voigt-Hill approach[S45] is obtained. Comparable bulk moduli have been calculated for $Li_{10}MP_2S_{12}$ (M = Si, Ge, Sn) and Li_6PS_5X (X = Cl, Br, I) (see Table S7).

Table S6: Averaged stiffness tensor C_{ij} (all entries in GPa) of t-Li_7SiPS_8, obtained from the stiffness tensors of four structural models of t-Li_7SiPS_8 with different PS_4^{3-}/SiS_4^{4-} arrangements. With partially occupied sites, the space group of t-Li_7SiPS_8 is $P42/nmc$.[S15] Hence, the entries of C_{ij} that are put in brackets are expected to vanish. The explicit distribution of PS_4^{3-}/SiS_4^{4-} tetrahedra as well as the distribution of Li ions, however, formally lower the symmetry of the structural models in almost all cases. As a result, several entries in C_{ij} become non-zero. These entries, however, are all below 1 GPa and therefore negligibly low compared to the proper entries of a tetragonal system with $P42/nmc$ space group.

$$C_{ij} = \begin{bmatrix} \mathbf{38.5} & \mathbf{26.4} & \mathbf{13.5} & (0.7) & (-0.4) & (0.2) \\ \mathbf{26.4} & \mathbf{41.7} & \mathbf{15.4} & (-0.1) & (-0.4) & (0.3) \\ \mathbf{13.5} & \mathbf{15.4} & \mathbf{40.5} & (0.9) & (0.1) & (-0.2) \\ (0.7) & (-0.1) & (0.9) & \mathbf{11.4} & (0.3) & (0.2) \\ (-0.4) & (-0.4) & (0.1) & (0.3) & \mathbf{9.6} & (0.7) \\ (0.2) & (0.3) & (-0.2) & (0.2) & (0.7) & \mathbf{17.8} \end{bmatrix}$$

Table S7: Calculated bulk modulus (B), Young's modulus (E), shear modulus (G), Poisson's ration (ν), and Pugh's ratio (G/B) of selected argyrodite and LGPS-type thiophosphate ion conductors based on the Reuss-Voigt-Hill approach. The values are taken from the references in column *Ref.* †The value in brackets was obtained from fitting energy-volume curves to the Birch-Murnaghan equation of state.

Compound	B / GPa	E / GPa	G / GPa	ν	G/B	Ref.
t-Li_7SiPS_8	23.5 (22.8)†	29.5	11.4	0.29	0.49	this work
$Li_{10}GeP_2S_{12}$	30.36	37.19	14.35	0.30	0.47	S46
$Li_{10}GeP_2S_{12}$	27.3	21.7	7.9	0.37	0.29	S47
$Li_{10}SiP_2S_{12}$	27.8	24.8	9.2	0.35	0.33	S47
$Li_{10}SnP_2S_{12}$	23.5	29.1	11.2	0.29	0.48	S47
Li_6PS_5Cl	28.7	22.1	8.1	0.37	0.28	S47
Li_6PS_5Br	29.0	25.3	9.3	0.35	0.32	S47
Li_6PS_5I	29.9	30.0	11.3	0.33	0.38	S47

Densities of Pressed Argyrodite Pellets - A Metadata Analysis

Although the importance of pellet density and preparation pressure is well known, few studies have addressed the influence of these two factors on the conductivity of thiophosphate-based solid electrolytes. Recently, Ohno and others published a laboratory comparative study that included such metadata. However, they focused only on the effects on ionic conductivity and activation energy. Figure S19 shows the relative pellet densities as a function of the pelletizing pressure. While intuition suggests higher pellet density with pressure, the data presented in Figure S19 do not show a positive trend in pellet density with pelletizing pressure. In fact, pellet density fluctuates around an average value of about 85%, with outliers $> 100\%$ (nonphysical value) and $< 70\%$. This metadata analysis indicates that applied pelletizing pressure is not an appropriate descriptor of the achievable pellet density. However, for some materials used in the study by Ohno *et. al.*, ionic conductivity shows a positive trend with increasing pellet density, while no such trend is observed for pelletizing pressure.

Since the bulk (B) and elastic (E) modulus, as well as the G/B ratio of aryrodites, such as Li_6PS_5Cl, and the *t*-Li_7SiPS_8 prototype, $Li_{10}GeP_2S_{12}$, is comparable (see Table S7), we expect similar high pressure densification behavior of the two classes of materials. Both materials meet Pugh's criterion for a ductile material ($B/G < 0.5$),[S48] undergoing plastic deformation rather than fragmentation under stress.

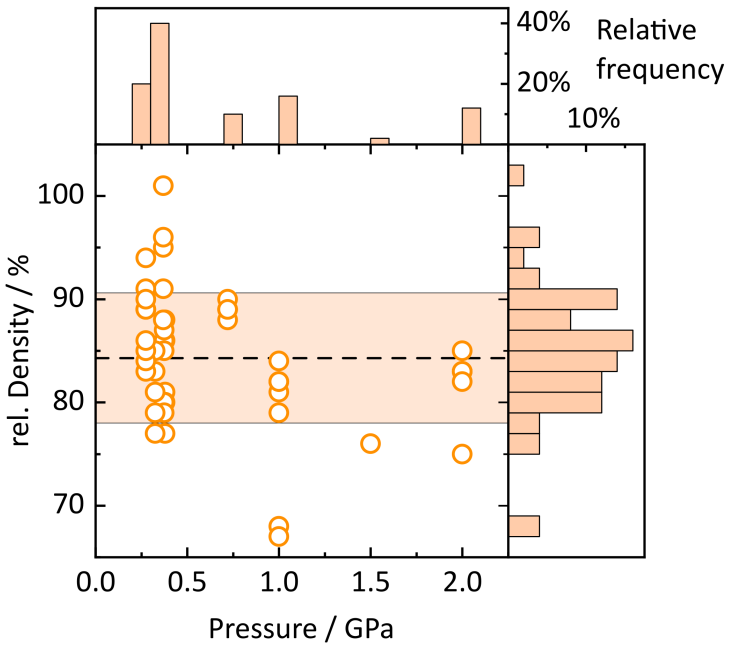

Figure S19: Relative density of pellets prepared from $Li_{6.6}P_{0.4}Ge_{0.6}PS_5I$, Li_6PS_5Cl, $Li_6PS_5Br_{0.75}I_{0.25}$, $Li_6PS_5Br_{0.25}I_{0.75}$, and Li_6PS_5I at different pressures. The data was extracted from the ESI of Ohno *et al.*[S49] The average density and the standard deviation is shown as a horizontal dashed line and light orange region, respectively.

References

(S1) Legland, D.; Arganda-Carreras, I.; Andrey, P. MorphoLibJ: integrated library and plugins for mathematical morphology with ImageJ. Bioinformatics **2016**, btw413.

(S2) Landini, G. Novel context-based segmentation algorithms for intelligent microscopy. accessed 11.04.2022; `https://blog.bham.ac.uk/intellimic/g-landini-software/`.

(S3) Clark, M. W. Quantitative shape analysis: A review. J. Int. Assoc. Math. Geol. **1981**, 13, 303–320.

(S4) Russ, J. The Image Processing Handbook, 4th ed.; CRC Press: Boca Raton, FL, 2002.

(S5) Cooper, A. R.; Eaton, L. E. Compaction Behavior of Several Ceramic Powders. J. Am. Ceram. Soc. **1962**, 45, 97–101.

(S6) Wünsch, I.; Finke, J.; John, E.; Juhnke, M.; Kwade, A. A Mathematical Approach to Consider Solid Compressibility in the Compression of Pharmaceutical Powders. Pharmaceutics **2019**, 11, 121.

(S7) Famprikis, T.; Kudu, Ö. U.; Dawson, J. A.; Canepa, P.; Fauth, F.; Suard, E.; Zbiri, M.; Dambournet, D.; Borkiewicz, O. J.; Bouyanfif, H.; Emge, S. P.; Cretu, S.; Chotard, J.-N.; Grey, C. P.; Zeier, W. G.; Islam, M. S.; Masquelier, C. Under Pressure: Mechanochemical Effects on Structure and Ion Conduction in the Sodium-Ion Solid Electrolyte Na_3PS_4. J. Am. Chem. Soc. **2020**, 142, 18422–18436.

(S8) Jeffery, R. N.; Lazarus, D. Calculating Activation Volumes and Activation Energies from Diffusion Measurements. J. Appl. Phys. **1970**, 41, 3186–3187.

(S9) Allen, P. C.; Lazarus, D. Effect of pressure on ionic conductivity in rubidium silver iodide and silver iodide. Phys. Rev. B **1978**, 17, 1913–1927.

(S10) Samara, G. A. Solid State Phys.; Elsevier, 1984; pp 1–80.

(S11) Fleig, J. The influence of non-ideal microstructures on the analysis of grain boundary impedances. Solid State Ion **2000**, 131, 117–127.

(S12) Fleig, J.; Maier, J. Finite-Element Calculations on the Impedance of Electroceramics with Highly Resistive Grain Boundaries: I, Laterally Inhomogeneous Grain Boundaries. J. Am. Ceram. Soc. **2004**, 82, 3485–3493.

(S13) Dankat, G. G.; Dumitran, L. M. Computation of the Electrical Resistance of a Low Current Multi-Spot Contact. Materials **2022**, 15, 2056.

(S14) Schneider, C. A.; Rasband, W. S.; Eliceiri, K. W. NIH Image to ImageJ: 25 years of image analysis. Nat. Methods **2012**, 9, 671–675.

(S15) Harm, S.; Hatz, A.-K.; Moudrakovski, I.; Eger, R.; Kuhn, A.; Hoch, C.; Lotsch, B. V. Lesson Learned from NMR: Characterization and Ionic Conductivity of LGPS-like Li_7SiPS_8. Chem. Mater. **2019**, 31, 1280–1288.

(S16) Harris, R. K.; Becker, E. D.; de Menezes, S. M. C.; Goodfellow, R.; Granger, P. NMR Nomenclature: Nuclear Spin Properties and Conventions for Chemical Shifts. IUPAC Recommendations 2001. Solid State Nucl. Magn. Reson. **2002**, 22(4), 458–483.

(S17) Massiot, D.; Fayon, F.; Capron, M.; King, I.; Le Calvé, S.; Alonso, B.; Durand, J.-O.; Bujoli, B.; Gan, Z.; Hoatson, G. Modelling one- and two-dimensional solid-state NMR spectra. Magn. Reson. Chem. **2002**, 40, 70–76.

(S18) Meier, C.; Weissbach, R.; Weinberg, J.; Wall, W. A.; Hart, A. J. Modeling and characterization of cohesion in fine metal powders with a focus on additive manufacturing process simulations. Powder Technology **2019**, 343, 855–866.

(S19) Meier, C.; Weissbach, R.; Weinberg, J.; Wall, W. A.; Hart, A. J. Critical influences of

particle size and adhesion on the powder layer uniformity in metal additive manufacturing. J. Mater. Process. Technol. **2019**, 266, 484–501.

(S20) Cundall, P. A.; Strack, O. D. L. A discrete numerical model for granular assemblies. Géotechnique **1979**, 29, 47–65.

(S21) Luding, S. About contact force-laws for cohesive frictional materials in 2D and 3D. Behavior of granular media **2006**, 9, 137–147.

(S22) Luding, S. Cohesive, frictional powders: contact models for tension. Granular Matter **2008**, 10, 235–246.

(S23) Parteli, E. J. R.; Pöschel, T. Particle-based simulation of powder application in additive manufacturing. Powder Technol. **2016**, 288, 96–102.

(S24) Nan, W.; Pasha, M.; Ghadiri, M. Numerical simulation of particle flow and segregation during roller spreading process in additive manufacturing. Powder Technol. **2020**, 364, 811–821.

(S25) Tsuji, Y.; Kawaguchi, T.; Tanaka, T. Discrete particle simulation of two-dimensional fluidized bed. Powder Technol. **1993**, 77, 79–87.

(S26) Blau, P. Friction Science and Technology: From Concepts to Applications, Second Edition; Mechanical Engineering; CRC Press, 2008.

(S27) Latz, A.; Zausch, J. Thermodynamic consistent transport theory of Li-ion batteries. J. Power Sources **2011**, 196, 3296–3302.

(S28) Danner, T.; Singh, M.; Hein, S.; Kaiser, J.; Hahn, H.; Latz, A. Thick electrodes for Li-ion batteries: A model based analysis. J. Power Sources **2016**, 334, 191–201.

(S29) Kresse, G.; Hafner, J. Ab initio molecular-dynamics simulation of the liquid-metal-amorphous-semiconductor transition in germanium. Phys. Rev. B **1994**, 49, 14251–14269.

(S30) Kresse, G. Ab initio molecular dynamics for liquid metals. J. Non Cryst. Solids **1995**, 192-193, 222–229.

(S31) Kresse, G.; Furthmüller, J. Efficiency of ab-initio total energy calculations for metals and semiconductors using a plane-wave basis set. Comput. Mater. Sci. **1996**, 6, 15–50.

(S32) Kresse, G.; Furthmüller, J. Efficient iterative schemes for ab initio total-energy calculations using a plane-wave basis set. Phys. Rev. B **1996**, 54, 11169–11186.

(S33) Perdew, J. P.; Burke, K.; Ernzerhof, M. Generalized Gradient Approximation Made Simple. Phys. Rev. Lett. **1996**, 77, 3865–3868.

(S34) Blöchl, P. E. Projector augmented-wave method. Phys. Rev. B **1994**, 50, 17953–17979.

(S35) Kresse, G.; Joubert, D. From ultrasoft pseudopotentials to the projector augmented-wave method. Phys. Rev. B **1999**, 59, 1758–1775.

(S36) Okhotnikov, K.; Charpentier, T.; Cadars, S. Supercell program: a combinatorial structure-generation approach for the local-level modeling of atomic substitutions and partial occupancies in crystals. J. Cheminform. **2016**, 8, 17.

(S37) Fu, Z.-H.; Chen, X.; Zhao, C.-Z.; Yuan, H.; Zhang, R.; Shen, X.; Ma, X.-X.; Lu, Y.; Liu, Q.-B.; Fan, L.-Z.; Zhang, Q. Stress Regulation on Atomic Bonding and Ionic Diffusivity: Mechanochemical Effects in Sulfide Solid Electrolytes. Energy Fuels **2021**, 35, 10210–10218.

(S38) Iwasaki, R.; Hori, S.; Kanno, R.; Yajima, T.; Hirai, D.; Kato, Y.; Hiroi, Z. Weak Anisotropic Lithium-Ion Conductivity in Single Crystals of $Li_{10}GeP_2S_{12}$. Chem. Mater. **2019**, 31, 3694–3699.

(S39) Chen, H.; Adams, S. Bond softness sensitive bond-valence parameters for crystal structure plausibility tests. IUCrJ **2017**, 4, 614–625.

(S40) Chen, H.; Wong, L. L.; Adams, S. SoftBV – a software tool for screening the materials genome of inorganic fast ion conductors. Acta Cryst. B **2019**, 75, 18–33.

(S41) Wong, L. L.; Phuah, K. C.; Dai, R.; Chen, H.; Chew, W. S.; Adams, S. Bond Valence Pathway Analyzer—An Automatic Rapid Screening Tool for Fast Ion Conductors within softBV. Chem. Mater. **2021**, 33, 625–641.

(S42) Qi, J.; Banerjee, S.; Zuo, Y.; Chen, C.; Zhu, Z.; Holekevi Chandrappa, M. L.; Li, X.; Ong, S. P. Bridging the gap between simulated and experimental ionic conductivities in lithium superionic conductors. Mater. Today Phys. **2021**, 21, 100463.

(S43) Murnaghan, F. D. The Compressibility of Media under Extreme Pressures. Proceedings of the National Academy of Sciences **1944**, 30, 244–247.

(S44) Birch, F. Finite Elastic Strain of Cubic Crystals. Phys. Rev. **1947**, 71, 809–824.

(S45) Toonder, J. M. J. d.; Dommelen, J. A. W. v.; Baaijens, F. P. T. The relation between single crystal elasticity and the effective elastic behaviour of polycrystalline materials: theory, measurement and computation. Model. Simul. Ma.t Sci. Eng. **1999**, 7, 909–928.

(S46) Wang, Z.-Q.; Wu, M.; Liu, G.; Lei, X.; Xu, B.; Ouyang, C. Elastic Properties of New Solid State Electrolyte Material $Li_{10}GeP_2S_{12}$: A Study from First-Principles Calculations. IInt. J. Electrochem. Sci. **2014**, 9, 562–568.

(S47) Deng, Z.; Wang, Z.; Chu, I.-H.; Luo, J.; Ong, S. P. Elastic Properties of Alkali Superionic Conductor Electrolytes from First Principles Calculations. J. Electrochem. Soc. **2016**, 163, A67–A74.

(S48) Pugh, S. XCII. Relations between the elastic moduli and the plastic properties of polycrystalline pure metals. London Edinburgh Philos. Mag. J. Sci. **1954**, 45, 823–843.

(S49) Ohno, S.; Bernges, T.; Buchheim, J.; Duchardt, M.; Hatz, A.-K.; Kraft, M. A.; Kwak, H.; Santhosha, A. L.; Liu, Z.; Minafra, N.; Tsuji, F.; Sakuda, A.; Schlem, R.; Xiong, S.; Zhang, Z.; Adelhelm, P.; Chen, H.; Hayashi, A.; Jung, Y. S.; Lotsch, B. V.; Roling, B.; Vargas-Barbosa, N. M.; Zeier, W. G. How Certain Are the Reported Ionic Conductivities of Thiophosphate-Based Solid Electrolytes? An Interlaboratory Study. ACS Energy Lett. **2020**, 5, 910–915.